

Capillary viscous flow and melting dynamics: Coupled simulations for additive manufacturing applications

Michael Blank^a, Prapanch Nair^{a,*}, Thorsten Pöschel^a,

^a Institute for Multiscale Simulation, Friedrich-Alexander Universität Erlangen-Nürnberg, Erlangen.

Abstract

The rate of melting of a solid and the rate of deformation of the resulting melt due to capillary forces are comparable in additive manufacturing applications. This dynamic structural change of a melting solid is extremely challenging to study experimentally. Using meshless numerical simulations we show the influence of the flow of the melt on the heat transfer and resulting phase change.

We introduce an accurate and robust Incompressible Smoothed Particle Hydrodynamics (ISPH) method to simulate melting of solids and the ensuing fluid-solid interaction. We present validations for the heat transfer across the free surface and the melting interface evolution, separately. We then present two applications for this coupled multiphysics simulation method—the study of rounding of an arbitrarily shaped particle during melting and the non-linear structural evolution of three spheres undergoing agglomeration. In both the studies we use realistic transport and thermal properties for the materials so as to demonstrate readiness of the method for solving engineering problems in additive manufacturing.

Key words: Additive manufacturing, Incompressible Smoothed Particle Hydrodynamics, phase change, latent heat, melting dynamics

1. Introduction

The evolution of topology in melting system, such as encountered in additive manufacturing applications, is often studied by decoupling the time scales of the flow of the melt and the phase change. Either static material properties are assumed, approximating the solids as highly viscous fluids [15] or assuming no flow following melting [32]. As the scope of additive manufacturing widens, there is an increasing need to resolve the tight coupling between flow of the melt and the phase change in order to achieve expected strength of the material. For serious engineering applications, uniformity in density and strength of the manufactured parts demand a micro mechanical understanding of the structural evolution during successive melting and solidification the material undergoes several times. Experimental studies at such spatial and temporal resolutions may be expensive [10], not to mention the high temperature conditions in which measurements need to be made. Traditional mesh based numerical approaches based on the Eulerian description (such as the Finite Volume Method)

*Principal corresponding author

Email addresses: prapanch.nair@fau.de (Prapanch Nair)

require special interface advection schemes (such as the Volume of Fluid method [12]) for fluid–fluid interfaces and Immersed Boundary [20] methods for evolving fluid–solid interface. These methods are challenged by large density ratios and the need for explicit conservation of mass, respectively. Mesh based methods based on the Lagrangian description (such as the Finite Element Method), on the other hand, are challenged by large deformations that require complex mesh treatments during the course of the simulation [2]. This is inherently due to the need to maintain the neighbor connectivity information between the computational nodes. In either case, generation of an efficient mesh requires considerable time and skill, especially in case of problems with evolving geometries. Meshless methods hold several advantages for such multi-physics applications.

Smoothed Particle Hydrodynamics (SPH) is a meshfree updated-Lagrangian method which was introduced by Gingold and Monaghan [9] and Lucy [17] for treating astrophysical phenomena and gas dynamics. Since the method is free from the need for the mesh connectivity information, many problems with complex interfaces and discontinuities in the domain are effectively solved by the method, making it a practical tool for multiphysics problems. For example, Monaghan presented an impressive SPH simulation of a methane gas bubble toppling a trawler to explain the sinking of ships in Witches Hole in the North sea [18]. This multiphysics simulation coupled two phase flow with free surface to an interacting rigid body. Heat transfer [22], phase change [8], and capillary flows [23] are solved separately using the method and are being continuously applied to a wide variety of engineering problems.

To successfully couple heat transfer, phase change and capillary flows in the context of additive manufacturing applications, each of these modules need to be improved and validated for appropriate boundary conditions (BC). Heat transfer is solved in SPH using the passive scalar approach for temperature [22]. The definition of accurate second order derivatives with discontinuous transport coefficients makes it applicable to realistic problems. Heat transfer from an ambient constant (or time varying) temperature needs to be implemented as a Dirichlet BC for temperature. A thin layer of SPH particles may be used for such BCs, but this would deteriorate the order of accuracy of the method itself. Hence, for problems involving continuous deformation, we present a free surface Dirichlet BC that is quite similar to the free surface Dirichlet BC for pressure in an earlier work [24].

Heat transfer—through conduction and convection due to capillary flow—effects phase change based on the latent heat capacity of the material. Phase change in a static domain has been solved using SPH [8] using a temperature as a passive scalar undergoing diffusion. Enthalpy based formulations have also been used for solving heat transfer in SPH [8] as an alternative approach. However, this involves computations of higher order derivatives than the temperature based approach. Using the free surface Dirichlet BC for temperature, the temperature based heat transfer model is used here to drive the phase change. A suitable capillary force model at the free surface is necessary to drive the flow and thereby cause convective transport of temperature. Capillary forces can be implemented in SPH using either continuum surface force (CSF) based models [1], geometric reconstruction of the interfaces [38] or using pairwise forces [34, 23]. Continuum models were developed for two fluid interfaces, and require special treatment for single fluid formulations with free surfaces [7]. The geometric models require robust, often expensive, reconstruction of interfaces from discrete particles for stable behaviour. For free surfaces we find the pairwise force model to be more amenable, since free surface and wetting phenomena are readily captured using this

approach. Recently, the pairwise force model was applied to dynamic capillary phenomena [23] in the Incompressible SPH (ISPH) method to show how additional damping may result from superimposing molecular length scales on a continuum model, and a restriction on the minimum smoothing resolution that is necessary to avoid this artificial damping. Different dynamic capillary flows involving free surfaces were demonstrated in this work. Other suitable capillary models may also be implemented in this context.

Multiphysics approaches for such tightly coupled phase change problems have also been solved using mesh based methods such as the finite volume method [11] and the finite element method [30, 5, 28]. In [11], the volume of fluid (VoF) method was used to characterize free surfaces of the flow resulting from a laser beam melting (LBM) process. In [28] a selective electron beam melting process, taking into account thermomechanical coupling and high temperature gradients in multiple time and length scales using a continuum assumption for the bed of particles, was considered. However, to our knowledge a melting model that takes into account the fluid-solid interaction with all degrees of freedom of the solids has not been attempted using mesh based methods in the context of additive manufacturing applications. Hence, we find that meshless methods such as SPH, where fluid solid interactions are easier to model owing to inherent mass conservation across the interface, could be a valuable addition. We have limited the scope of the current work to conduction and convection heat transfer (due to the melt flow) and assume negligible thermal gradients and therefore a constant surface tension coefficient. We systematically introduce and validate heat transfer and phase change to the flow solver to eventually solve fully coupled problems within this scope.

This paper is organized as follows. In Sec. 2, we present the heat transfer, phase change and capillary flow models with the respective governing equations. In Sec. 3 we present numerical implementation of these models to the ISPH method. Here we introduce our BC for heat transfer across the free surface. We also separately validate the heat transfer across free surface and the melting of a solid for different latent heat values in 2D and 3D. In Sec. 4 we present applications of this method to representative problems in additive manufacturing. We compare the melting rate of a complex shaped solid particle with theoretical results for the melting of a spherical solid to appreciate the influence of shape on the capillary viscous flow on the heat transfer in the melting particle. Finally, we simulate the agglomeration of a chain of three solid spheres undergoing melting with two different sets of material properties to show the shape evolution is a result of instabilities relating to the solid–liquid interaction during the melting process.

2. Governing Equations

We assume the fluid (melt) and the solid to be incompressible, with negligible density variation during the phase change. The transient heat transfer in the system is governed by the enthalpy equation,

$$\frac{\partial H}{\partial t} = \nabla \cdot (k \nabla T), \quad (1)$$

where H is the enthalpy, k is the thermal conductivity of the material and T is the temperature. For an incompressible medium, the enthalpy H can be written as a function of

temperature. Therefore,

$$\frac{dH}{dT} \frac{\partial T}{\partial t} = \nabla \cdot (k \nabla T). \quad (2)$$

Here dH/dT is the specific heat capacity at constant pressure, C .

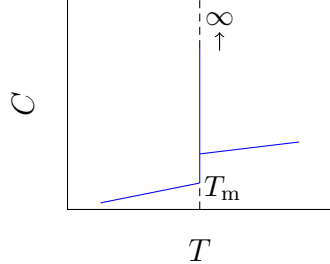


Figure 1: Sketch of the specific heat to temperature dependence during a melting process.

Phase change (melting and solidification) can be modelled using Eq. 2 by defining an effective heat capacity [8] which increases (or decreases) by the latent heat of melting (or solidification), L , of the material at a melting (or solidifying) interface. This effective heat capacity can be defined as

$$C_{\text{eff}} = \begin{cases} C_s & T < T_m \\ C_m + L\delta(T - T_m) & T = T_m \\ C_l & T > T_m \end{cases} \quad (3)$$

where $\delta(T - T_m)$ is the Dirac delta function, C_s and C_l are the specific heat capacities of the material in the solid and liquid phases, respectively, and C_m is the specific heat capacity of the material at the melting temperature. This model relating the heat capacity to the temperature and the latent heat is schematically shown in Fig. 1.

The liquid domain formed from the melting process is modelled using a one-fluid formulation, neglecting the presence of air and is governed by the incompressible Navier–Stokes equation given by:

$$\frac{d\mathbf{u}}{dt} = -\frac{1}{\rho} \nabla P + \nabla \cdot \left(\frac{\mu}{\rho} \nabla \mathbf{u} \right) + \mathbf{f}^{\text{int}} + \mathbf{f}^B. \quad (4)$$

Here P is the pressure, μ is the coefficient of viscosity, \mathbf{f}^{int} is the interfacial force acting at the free surface and at the liquid–solid interface and \mathbf{f}^B is the body force per unit mass acting on the fluid. The solid that undergoes melting is assumed to be rigid and interacts with the liquid domain through stresses at the interface.

The pressure is given by $P = p + \tilde{p}$, where p is the hydrodynamic pressure and \tilde{p} is any constant background pressure which does not contribute to the pressure gradient force due to incompressibility of the medium. The hydrodynamic pressure p is not coupled to the density and serves to ensure an incompressibility constraint such as a zero divergence velocity field

$$\nabla \cdot \mathbf{u} = 0, \quad (5)$$

or equivalently, an isochoric deformation given by a unit determinant of the deformation gradient tensor, \mathbf{F} [25]:

$$\det(\mathbf{F}) = 1. \quad (6)$$

The numerical implementation of models for heat transfer, phase change, capillary fluid flow and the solid-fluid interaction based on ISPH is explained henceforth.

3. SPH implementation and validation

The SPH method is based on discrete computational nodes that carry field variable values and interact with each other within a cut-off radius associated with each node. A smoothing function, W (also known as the kernel) and its derivatives are used to define continuous approximations of the field and its derivatives through convolution. Conservation of momentum is satisfied in the bulk through inter-SPH-particle forces obtained through the kernel approximations.

For an incompressible fluid, the SPH formulation for momentum conservation is [33]:

$$\begin{aligned} \frac{d\mathbf{u}}{dt}\Big|_a &= - \sum_b m_b \frac{p_a + p_b}{\rho_a \rho_b} \nabla_a W_{ab} \\ &\quad + \sum_b m_b \frac{\mu_a + \mu_b}{\rho_a \rho_b} F_{ab} \mathbf{u}_{ab} + \mathbf{f}_{ab}^{\text{int}} + \mathbf{f}_a^B, \end{aligned} \quad (7)$$

where m is the mass, ρ is the density, p is the hydrodynamic pressure, μ is the coefficient of viscosity and \mathbf{u} is the velocity at an SPH particle a or SPH particle b in the neighborhood of a . The function W is a radially symmetric and positive definite smoothing function (also known as the smoothing kernel) with a finite cut-off radius (for the SPH discretization) defined for an SPH particle pair as $W_{ab} = W(r_{ab}, h)$, where h is the smoothing length of the kernel. The gradient of the smoothing function appears as $\nabla_a W_{ab}$ for an SPH particle a with respect to its neighbor b . The radial derivative of the kernel, given by F_{ab} [21] is computed from the gradient of W as

$$F_{ab} = \frac{\mathbf{r}_{ab} \cdot \nabla_a W_{ab}}{r_{ab}^2 + \epsilon^2} \quad (8)$$

where ϵ is a small number introduced to avoid division by zero in the rare event of SPH particles overlapping in position and is usually set to $(0.01h)^2$.

The hydrodynamic pressure p in incompressible flows is nothing but a Lagrange multiplier that satisfies a constraint for incompressibility given by Eq. 5 or 6. For a divergence free velocity field, following grid based fluid simulation methods, pressure is obtained by solving the pressure Poisson equation (PPE),

$$\nabla \cdot \left(\frac{1}{\rho} \nabla p \right) = \frac{\nabla \cdot \mathbf{u}}{dt}. \quad (9)$$

In the discrete SPH domain, the above equation can be approximated as

$$\sum_b \frac{m_b}{\rho_b} \frac{4(p_a - p_b)}{\rho_a + \rho_b} F_{ab} = \sum_b \frac{m_b}{\rho_b} \frac{\mathbf{u}_{ab} \cdot \nabla_a W_{ab}}{\Delta t}. \quad (10)$$

This approximation with unknown pressure values, represents a simultaneous system of linear equations in the unknowns p_a , and can be solved numerically using a linear solver such as BiCGSTAB [31]. For a domain at least partly bounded by free surfaces, a Dirichlet BC for pressure can be semi-analytically applied by the following modification to this linear system [24]:

$$(p_a - p_o)\kappa - \sum_b \frac{m_b}{\rho_b} \frac{4p_b}{\rho_a + \rho_b} F_{ab} = \sum_b \frac{m_b}{\rho_b} \left(\frac{\mathbf{u}_{ab} \cdot \nabla_a W_{ab}}{\Delta t} - \frac{4p_o}{\rho_a + \rho_b} F_{ab} \right) \quad (11)$$

where p_o represents the ambient pressure and κ , given by

$$\kappa = \sum_{b_{\text{bulk}}} \frac{m_b}{\rho_b} \frac{4}{\rho_a + \rho_b} \frac{\mathbf{r}_{ab} \cdot \nabla_a W_{ab}}{r_{ab}^2 + \epsilon^2}, \quad (12)$$

is a factor which remains constant for a given domain with given smoothing parameters and constant density. This modification effectively applies a penalty term that accounts for the deficiency of the kernel for an SPH particle near the free surface, and does not add to the computational cost.

Capillary forces are modelled using a pairwise SPH particle force function $\mathbf{f}_{ab}^{\text{int}}$ based on the molecular theory of surface tension [29, 34] and is chosen to have an attractive part in the long range and a repulsive part in the short range. This capillary model is elaborated in a recent publication in the context of dynamic free surface flows [23]. We use the following pairwise force:

$$F_{\alpha\beta}^{\text{int}}(r_{ab}) = \begin{cases} -s_{\alpha\beta} \cos\left(\frac{3\pi}{4}q_{ab}\right) & q_{ab} = \frac{r_{ab}}{h'} \leq q_{\text{cutoff}} \\ 0 & q_{ab} = \frac{r_{ab}}{h'} > q_{\text{cutoff}}, \end{cases} \quad (13)$$

where α and β represent the phases of the SPH particles a and b , respectively. The strength of the pairwise force is given by $s_{\alpha\beta}$. Here the cut-off distance of the pairwise force is set to be the same as that of the smoothing kernel. The strength of the pairwise force for a given macroscopic surface tension can be predetermined [34] in the presence of a free surface and this relationship is [23]:

$$\sigma = \lambda s_{ll} h_r^4, \quad \text{for 2D and} \quad (14)$$

$$\sigma = \lambda s_{ll} \frac{h_r^5}{\Delta x} \quad \text{for 3D,} \quad (15)$$

respectively. Here, h_r is the ratio of the smoothing length of the kernel to the initial SPH particle spacing Δx (here we use a square lattice arrangement of SPH particles as the initial condition). Note that these expressions correspond to the specific choice of pairwise force function and compact support. The constant due to integration of the pairwise force function, λ takes the value 0.0476 in two dimensions and 0.0135π in three dimensions, respectively, for the interaction function given by Eq. 13 [23]. The contact angle (Θ) at the liquid–solid contact line is related to the pairwise force strengths [23] as

$$\cos \Theta = \frac{-s_{ll} + 2s_{ls}}{s_{ll}}, \quad (16)$$

where s_{ls} is the strength of the potential force between SPH particles belonging to the liquid and solid phase. For more information on the proper implementation of this pairwise force approach for dynamic problems, we direct the reader to [23].

We use an explicit viscous force approximation (the second term on the right hand side) that is extensively used in SPH literature [22] especially for low Reynolds number flows.

3.1. Heat transfer across free surface

Heat transfer problems have been solved in SPH using the approximation of second order derivatives. In finite domains, the kernel of SPH gets truncated at the interface. Our intended applications require ambient boundary conditions. This is achieved by a semi analytic Dirichlet BC for temperature similar to the application of Dirichlet pressure BC in the Laplacian of pressure presented in the previous section.

The heat transfer model (Eq. 2) is approximated in the SPH domain as follows:

$$C\rho \frac{dT}{dt} = \sum_b \frac{m_b}{\rho_b} \frac{4}{\rho_a + \rho_b} \left(\frac{k_a + k_b}{2} T_{ab} \right) F_{ab} \quad (17)$$

where, k_a and k_b represent the thermal conductivity at the SPH particle a and b , respectively and $T_{ab} = T_a - T_b$.

Following a similar approach to the free surface Dirichlet BC for the pressure Poisson equation [24] presented above in Eq. 11, Dirichlet boundary condition for temperature can be applied semi-analytically, as well. Applying this to the Eq. 2 leads to the following heat transfer equation approximation:

$$C\rho \frac{\partial T}{\partial t} \Big|_a = 2 \sum_b m_b \left(\frac{k_a + k_b}{\rho_a + \rho_b} (T_a - T_b) F_{ab} \right) + \kappa \frac{k_a + k_o}{2} \rho_a (T_a - T_o), \quad (18)$$

where κ is the same constant as in Eq. 12 and T_o is the ambient temperature (which can be time varying).

The accuracy of heat transfer is central to our problem and requires careful validation. For this, we solve the 2D heat conduction problem for a finite flat plate with two different sets of boundary conditions. In the first case in fig. (2) all four sides are modeled as free surfaces exposed to constant ambient temperature. The second setup in fig. (3) uses, aside from Dirichlet boundary conditions on three walls, an adiabatic fourth wall modeled by static SPH particles.

The heat conduction through the flat plate across the free surface is compared to the analytical solution at different times in Fig. 2 where the plate is heated at constant temperature from the ambience on all four sides. An array of 160×160 fixed SPH particles are used to represent a square flat plate of side $l = 0.1$ m. The ambient temperature is set to 0 K and the plate is set to a uniform initial temperature of 1 K. Throughout this paper, when no material property is dependent on temperature, only the gradient of temperature appears in the governing equations for heat transfer. Hence the temperature and the corresponding conditions for the phase change region can be shifted by an additive constant. Hence the use of 0 K here does not suggest the thermodynamic absolute zero. The density of the material is set to 1 kg m^{-3} and the thermal diffusivity is set to $1 \times 10^{-4} \text{ m}^2 \text{s}^{-1}$.

In Fig. 3, an adiabatic wall with a homogeneous Neumann BC for temperature is applied. The simulation results are compared to analytical solutions, available widely in standard text books on numerical methods [16], and a very good match is observed.

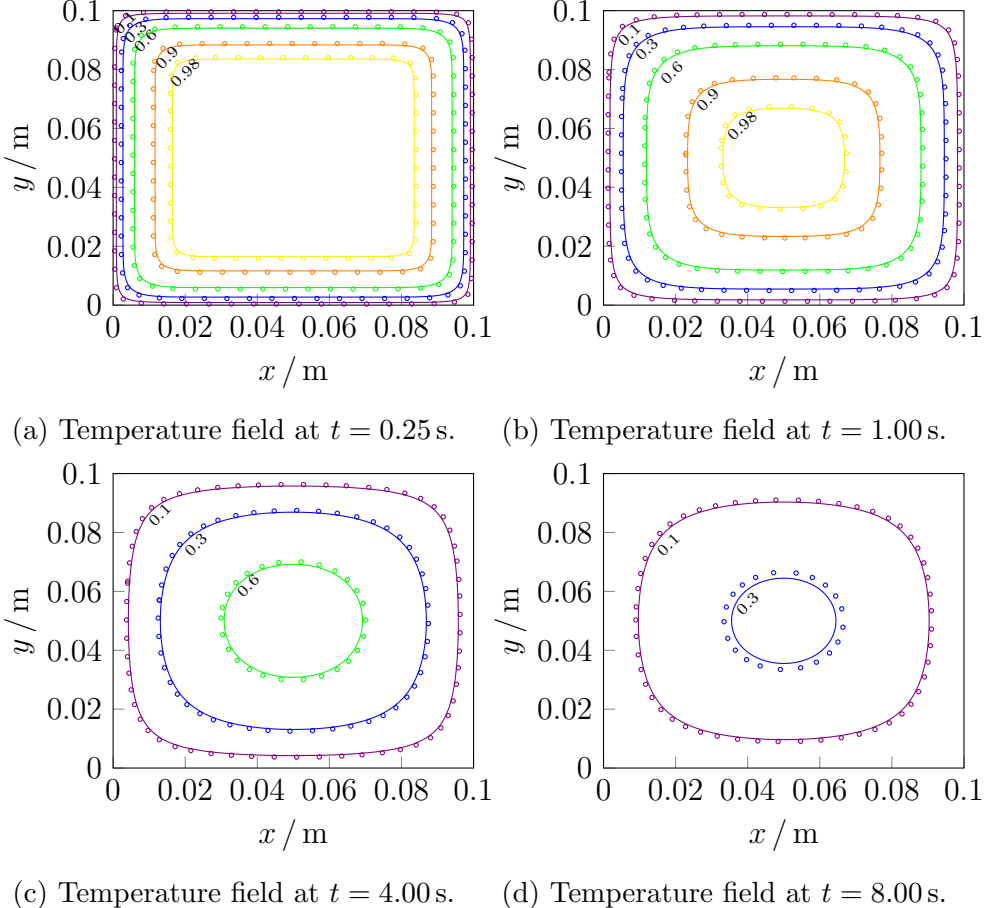


Figure 2: Evolution of the temperature profile within a square at different times for a resolution of 160×160 SPH particles with Dirichlet BC on all sides.

The consistency of this heat transfer model can be seen in Fig. 4, showing greater than first order accuracy. The L_2 norm of the error at different times are presented against the resolution of the domain. The order of accuracy of the heat transfer simulation with the free surface BC can be clearly seen to be more than first order in Fig. 4.

3.2. Static phase change

Phase change is modelled using the effective heat capacity C_{eff} defined in Eq. 3. There are different strategies for implementing the effect of latent heat into a numerical method. On the one hand it can be added as a source term to the heat conduction equation [37, 26] or, on the other hand, by modifying the heat capacity itself [8, 35, 13]. In this work an integral interpolation introduced by [8] is implemented to modify the heat capacity in order to model phase change processes. Therefore, the model for a smoothed latent heat in SPH can be derived by starting from the definition of an effective heat capacity C_{eff} which includes the effect of latent heat [4, 14] given by Eq. 3. This formulation is composed of the heat capacities for solid C_s and C_l liquid phase as well as the heat capacity within the phase change region C_m . Here, C_{eff} at the melting temperature T_m includes the total latent heat

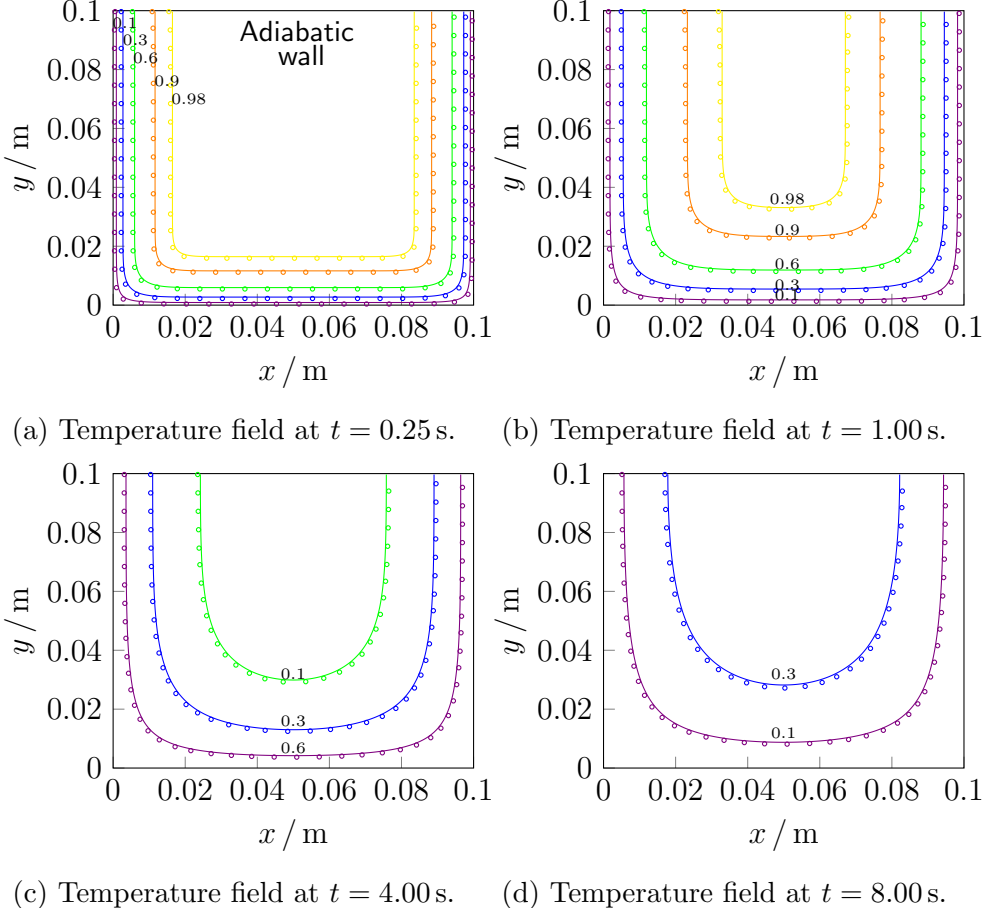


Figure 3: Evolution of the temperature profile within a square at different times for a resolution of 160×160 SPH particles with Dirichlet BC on three sides and Neumann on the fourth.

of the phase change, $L = \int_{-\infty}^{\infty} L\delta(T - T_m)$.

The Dirac function can be replaced in the one-dimensional temperature domain by a kernel function W_T with smoothing length h_T analogous to the spatial kernel function in SPH resulting in:

$$C_{\text{eff}} = \begin{cases} C_s & T < T_m - \Delta T \\ C_m + LW_T(T - T_m, h_T) & T_m - \Delta T \leq T \leq T_m + \Delta T \\ C_l & T > T_m + \Delta T \end{cases} \quad (19)$$

The temperature domain ΔT represents a mushy region around the phase change temperature. The size of this region is defined as the product of the smoothing length h_T and the maximum range of support q_{\max} of the temperature kernel.

$$\Delta T = h_T q_{\max}. \quad (20)$$

The outcome of this is a changing C_{eff} inside of this region with a maximum latent heat effect at the phase change temperature. The accuracy of this approach is further improved

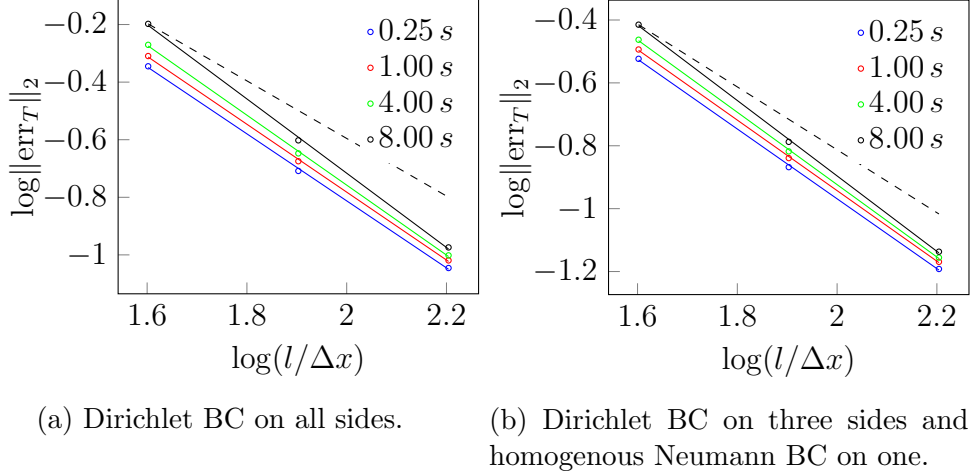


Figure 4: L_2 norm of the error in temperature (T) in the domain at different times and spatial resolutions. The plot shows the order of accuracy greater than 1 at all time instances. Dashed lines in both the plots indicate first order convergence, provided for reference.

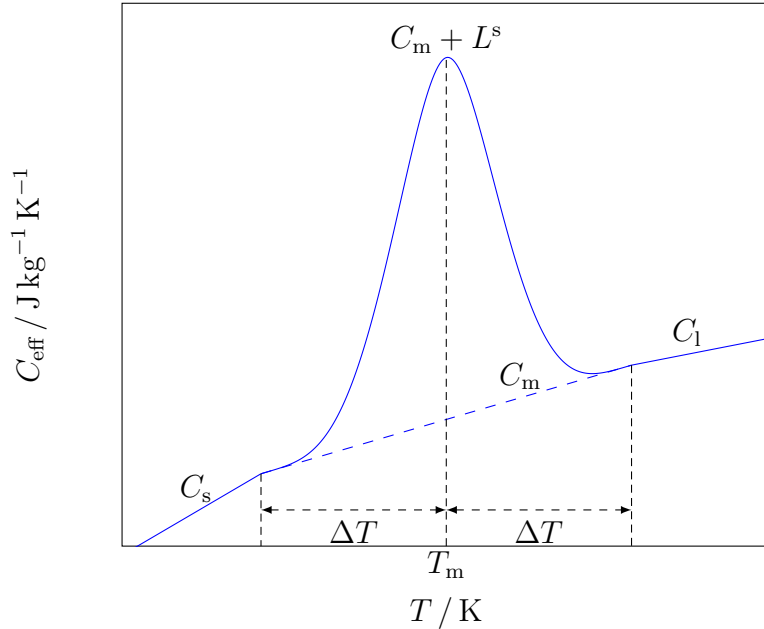


Figure 5: Smoothed effective heat capacity within the mushy region of the phase transition temperature. The increase in specific heat at the interface is $L^s = LW_T(T - T_m, h_T)$ in the mushy region.

by considering the distance between adjacent SPH particles and the temperature difference with respect to the transition temperature. This results in a smoothed latent heat L^s [8] for a SPH particle a defined as

$$L_a^s = \sum_b \frac{m_b}{\rho_b} (LW_T(T_b - T_m, h_T)) W(\mathbf{r}_b - \mathbf{r}_a, h). \quad (21)$$

This results in the effective heat capacity given in equation (22) which is replacing the

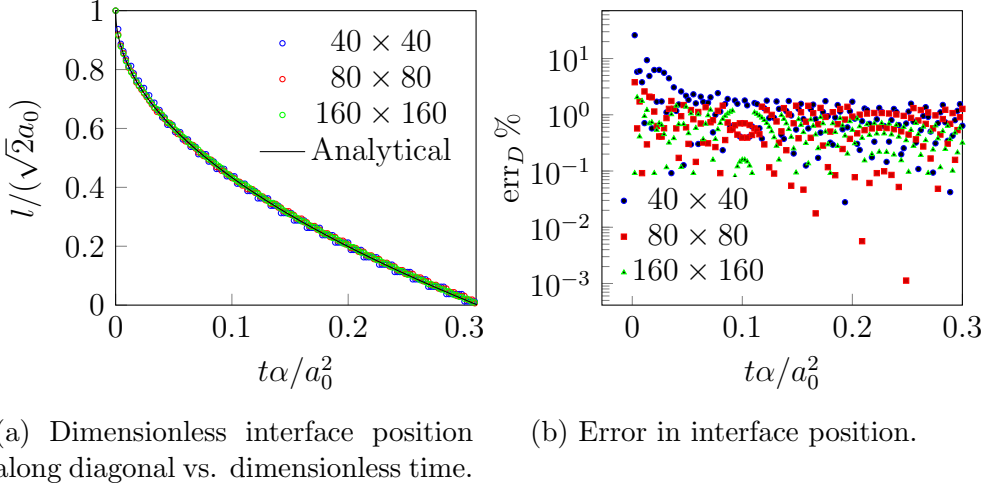


Figure 6: Neumann problem: Interface position (a) and calculated errors (b) obtained for different resolutions. The characteristic length a_0 is the side of the quarter of the square plate undergoing phase change.

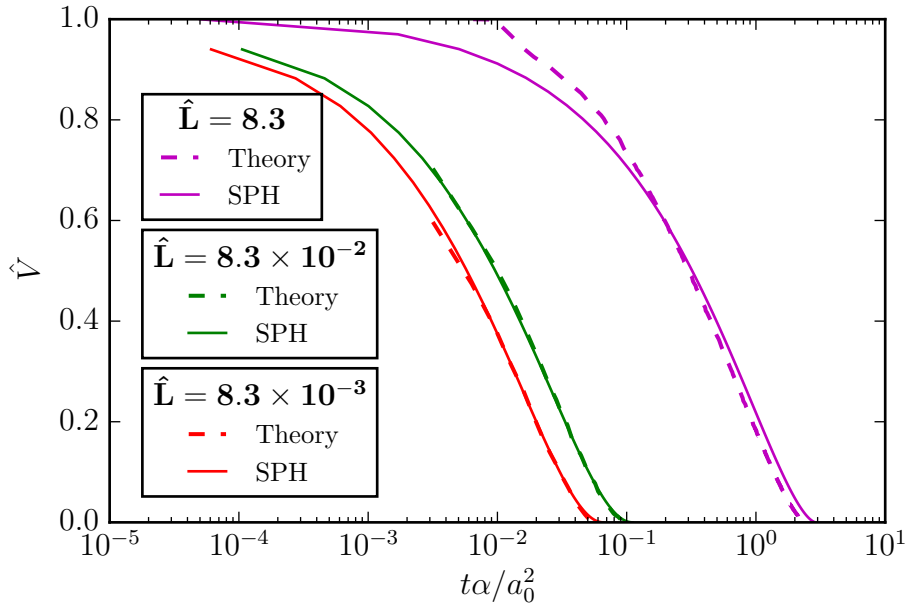


Figure 7: Static melting of a spherical solid—comparison of evolution of solid volume fraction with 1D axisymmetric theory. Here \hat{L} is the non-dimensionalized latent heat, $\hat{L} = L / (k_s(T_o - T_m))$.

specific heat capacity of the heat conduction equation (17).

$$C_{\text{eff}} = \begin{cases} C_s & T < T_m - \Delta T \\ C_m + L^s & T_m - \Delta T \leq T \leq T_m + \Delta T \\ C_l & T > T_m + \Delta T \end{cases} \quad (22)$$

The effective heat capacity augmented by the smoothed latent heat is shown in Fig. 5.

The phase change model in SPH together with the free surface BC for ambient temperature needs to be validated. Here we choose the Neumann problem in 2D [27] and the Stefan's problem in axisymmetric 3D [19] to validate the evolution of the melting interface with time.

In two dimensions, the two edges of a right angled corner of a 2D square plate is heated. The medium is set to a density of 1 kg/m^3 . The initial and melting temperature are set to 2.0 and 2.3 K respectively. The thermal conductivity and specific heat capacity of both phases were maintained at a value of 1 in SI units. The latent heat was set to 0.25 J/kg. Three different resolutions were considered corresponding to 40, 80 and 160 SPH particles along one direction in the quarter space of dimensions $a = 3 \text{ m}$. The choice of these parameters are arbitrary, since the aim of the validation is only to check the numerical approximation of the model. In the following section we will resort to more realistic simulation parameters. As the temperature rises above the melting temperature, the solid melts and the solid–liquid interface moves inwards. The location of the phase change interface along the diagonal, normalized by the width of the plate is plotted against non-dimensional time in Fig. 6a. The melting process is assumed to be static, such that the molten region is assumed to not deform. This problem is simulated without liquid deformation for different spatial resolutions and compared against the analytical solution. Note that the heat transfer across the free boundary is based on the semi-analytic boundary formulation in Eq. 11. The interface location appears as a stepped curve because of the discrete sampling in time. We see that the interface evolution is predicted accurately. In Fig. 6b we see the order of accuracy increases with increasing resolution, consistently. The discrete sampling in time makes it difficult to obtain the exact order of accuracy.

In 3D, we solve the Stefan's problem in a sphere and compare the results with the solutions of an axisymmetric model proposed in [19], given by

$$\frac{\partial h}{\partial \hat{t}} = \frac{\partial^2 \hat{T}}{\partial r^2} + \frac{2}{r} \frac{\partial \hat{T}}{\partial r} \quad \text{in } 0 < r < 1, \quad (23)$$

where r is the radial location in the unit sphere, normalized by the radius of the sphere, R . Time is normalized by R^2/k_s , where k_s is the thermal conductivity of the solid phase. The enthalpy H is related to the temperature \hat{T} (normalized by $(T_o - T_m)$) by

$$\hat{T} = \begin{cases} H - \beta, & H < 0 \\ 0, & 0 \leq H \leq \beta, \\ \tilde{k}(H - \beta), & H > \beta, \end{cases} \quad (24)$$

where β , the Stefan number is given by $\beta = L/(C_s(T_o - T_m))$, where C_s is the specific heat capacity of the solid phase. Also \tilde{k} represents the ratio of thermal diffusivities of the solid and liquid phases respectively, $\tilde{k} = k_l/k_s$. Eq. 23 is solved using finite difference method as given in [19] and [36]. We discretized the spatial derivatives using a central difference approximation and the temporal derivatives using forward time Euler approximation and solved the system explicitly to obtain the melting interface position in time.

In order to motivate application to realistic materials, we present the results for different latent heat spanning different orders of magnitude. Though the results presented are non-dimensionalized, the material parameters are chosen to resemble realistic materials and these

parameters will be used for further simulations in the dynamic context in the next section. In Fig. 7 we present the time evolution of the volume of the solid, \hat{V} , during melting. Instead of the location of the interface position, we present the volume of the solid remaining at different instances in time. Since our goal is to present the effect of shape of the melting body, we choose the volume of the solid instead of a linear dimension. The simulation and discretization parameters are presented in Table 1. Three different latent heat values are considered.

We see that for lower latent heat values, the match is accurate. However, for large latent heat values, the onset of melting is slightly different from the analytic solution. This is perhaps due to the truncated temperature and spatial kernel used in computing the latent heat. We will be addressing this in a future work.

Quantity	Value	Unit
σ	0.2308	Nm ⁻¹
Θ	30	°
μ	0.001793	Pas
ρ	1000	kg m ⁻³
T_{initial}	1	K
T_m	1.15	K
T_o	4.0	K
C	2.11	kJ kg ⁻¹ K ⁻¹
L	0.1, 1.0, 100.0	kJ kg ⁻¹
k_s, k_l	2.14	W m ⁻¹ K ⁻¹
Δx	4.0×10^{-5}	m
ΔT	0.1	K
R	5.66×10^{-4}	m

Table 1: Parameters used to simulate melting of a sphere and a mill particle.

The time update is numerically stable only when Δt satisfies the condition

$$\Delta t \leq \min_a \left(0.25 \frac{h}{3|\mathbf{u}_a|}, 0.25 \sqrt{\frac{m_a h}{3|\mathbf{f}_a^{\text{int}}|}}, 0.25 \frac{\rho h^2}{9\mu} \right). \quad (25)$$

4. Applications: Melting dynamics

The multiphysics SPH algorithm is implemented in an ISPH code [24, 25] and melting problems with flow dynamics are solved for complex shaped three dimensional solids. Results are compared with theoretical results and other numerical studies with simplistic assumptions.

4.1. Melting of a mill particle

A complex shaped geometry obtained by scanning a mill particle from an industrial process is shown in Fig. 8. This geometry is filled with SPH particles in a square lattice

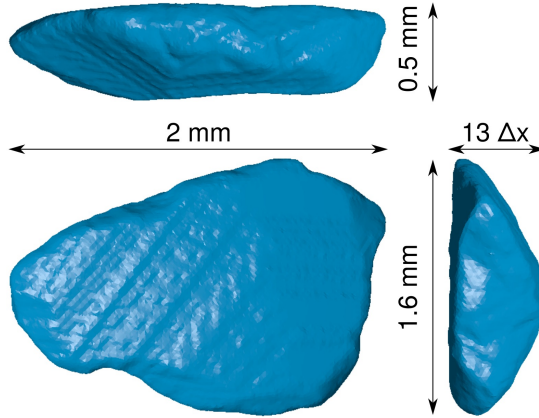


Figure 8: Dimensions of the complex shaped mill particle in mm. The initial discretization length between SPH particles is given by Δx .

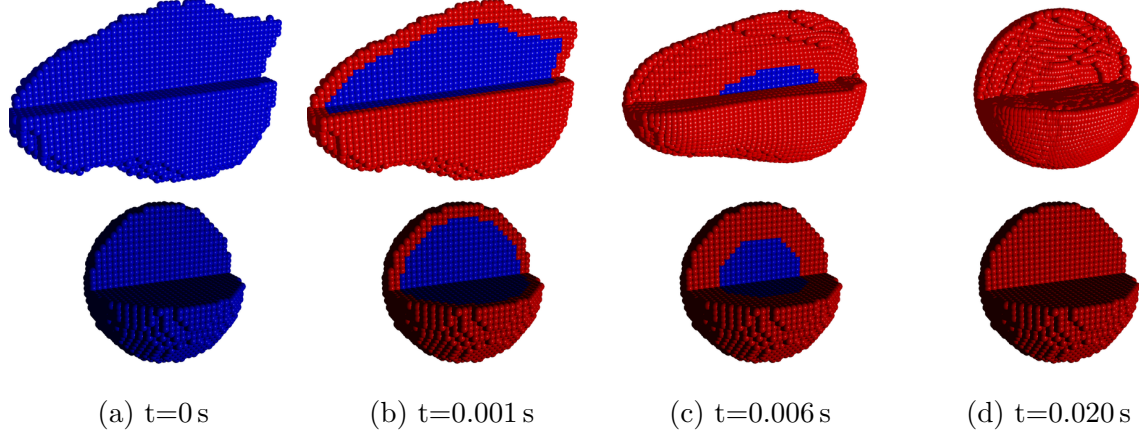


Figure 9: $L = 0.01 \text{ kJ/kg}$: Melting of an irregular shaped mill particle vs. a static sphere. Blue colored SPH particles denote solid and red colored SPH particles denote liquid phase.

with the same initial spacing and simulation parameters as that used in the melting of spheres presented in the previous section. Figure 8 also shows the dimensions of the particle and the SPH intial particle resolution for simulation in the smallest dimension ($\Delta x = 0.04 \text{ mm}$). The volume of the mill particle is chosen to be equal to the volume of the sphere in the previous section. We have avoided discontinuities in the thermal properties across the solid–liquid interface in order to compare with the theoretical results and to focus on the melting and capillary force based deformation as the first step. Discontinuities in the thermal properties will be introduced in the subsequent applications (Sec. 4.2) of the method.

The evolution of the solid and liquid phases are shown in Figs. 9–14. Since different physical processes are coupled in this simulation, we have not attempted to non-dimensionalize this system. However, the rate of phase change is non-dimensionalized in order to be compared with the melting of the sphere in the previous section.

In Figs. 9 and 10 blue and red SPH particles represent solid and liquid phases, respec-

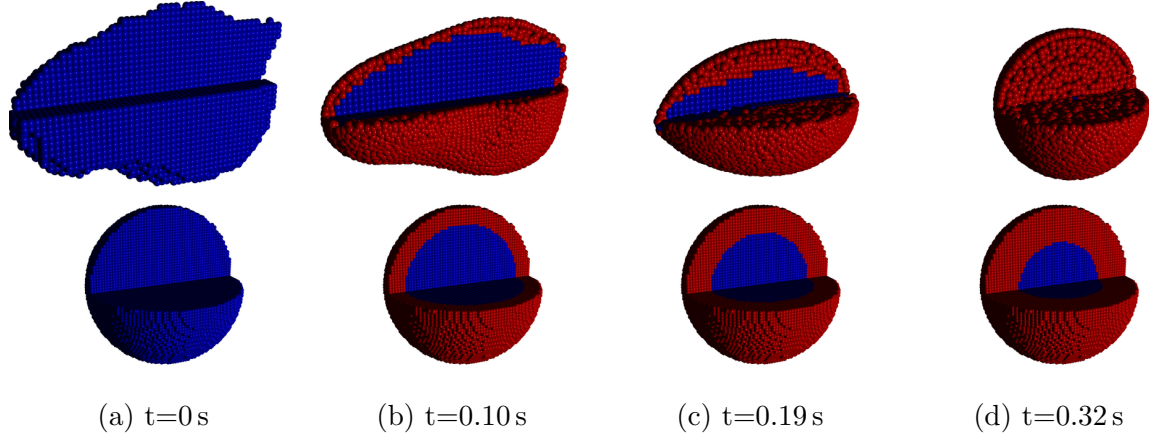


Figure 10: $L = 100.0 \text{ kJ/kg}$: Melting of an irregular shaped mill particle vs. a static sphere. Blue colored SPH particles denote solid and red colored SPH particles denote liquid state.

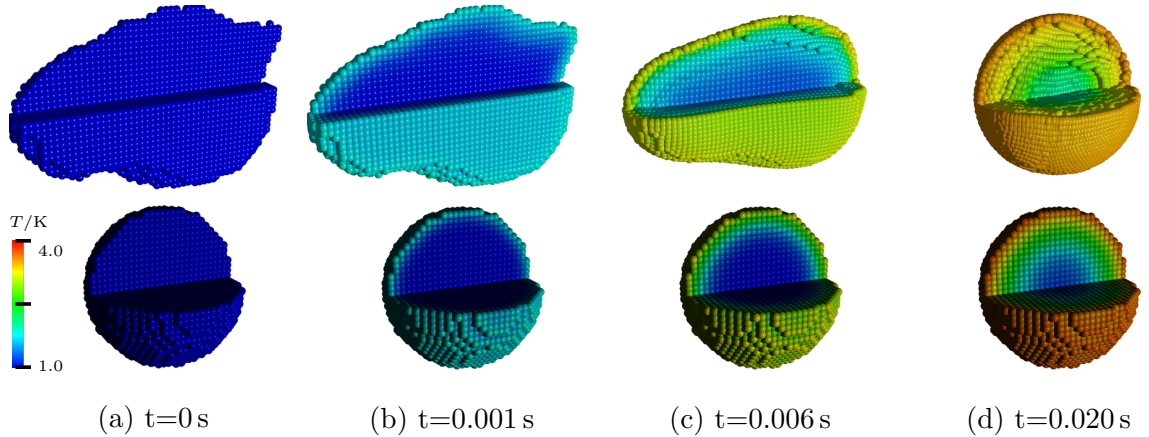


Figure 11: $L = 0.01 \text{ kJ/kg}$: Temperature profile in the melting mill particle.

tively. For better illustration, a quadrant is clipped out of the irregular particle to show the scalar field evolution in the bulk of the particle. At the beginning of the simulation, all SPH particles are in solid state. As a result of the heating from the constant ambient temperature, the phase change occurs as the temperature rises above the melting point. A layer with liquid SPH particles are formed at the surface of the mill particle after about 0.001 s for the latent heat of 0.01 kJ/kg and 0.10 s for the latent heat of 100 kJ/kg. The liquid–solid interface is hydrophilic owing to the acute contact angle of 30°. The contact angle due to homologous wetting between a molten metal and its solid counterpart is often assumed to be a function of the Stefan number [6], and can be a complex property to determine. We have therefore used an arbitrary hydrophilic contact angle in our simulations. Hence the unmelted solid remains wetted by the melt. Since the melting is slower for higher latent heat, the fluid relaxes more and this can be seen at 0.19 s in the large latent heat case, where the liquid has assumed a shape close to a prolate ellipsoid. For both the latent heat values considered, the surface roughness (resolved by the initial SPH particle resolution) smoothes

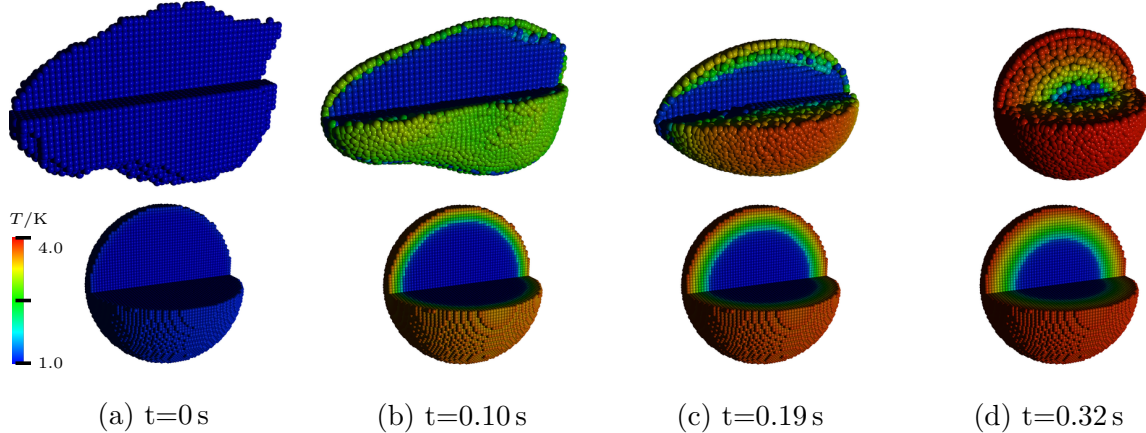


Figure 12: $L = 100.0 \text{ kJ/kg}$: Temperature field in the melting particles. Top row shows the mill particle with melt flow and the bottom row shows a static spherical particle.

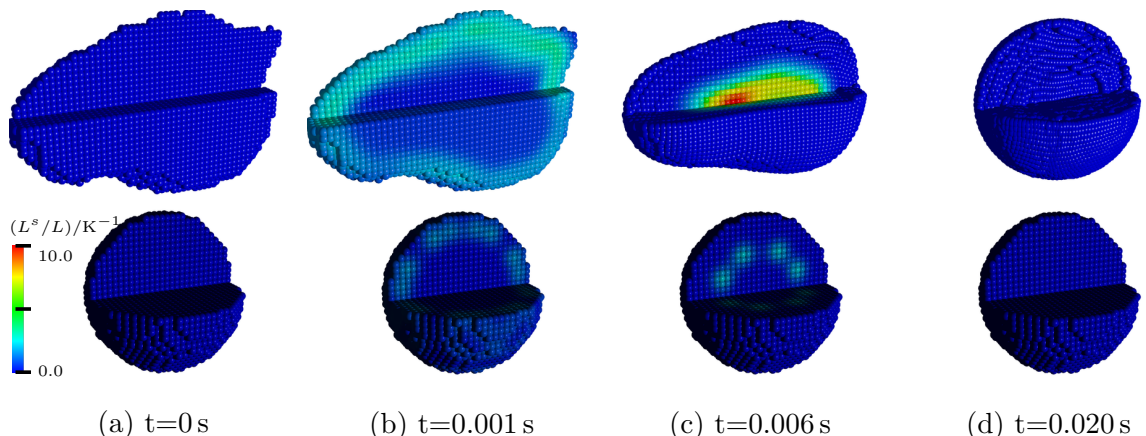


Figure 13: $L = 0.01 \text{ kJ/kg}$: Increase in heat capacity at the interface during the melting of the mill particle.

out differently, since the melting rate is faster than the capillary relaxation process for low latent heat value. Also, for low latent heat, the particle rounding takes place much later than the complete melting of the solid. Once it achieves the spherical shape the melt drop oscillates about its mean spherical shape. Such oscillation of a viscous fluid drop using the same pairwise force capillary model is validated against analytical results in [23].

In Figs. 11 and 12, the temperature field of the melting body is shown at different instances. With the onset of heat exchange with the ambiance the solid phase SPH particles start to heat up from the free surface. When the first layer of liquid SPH particles is formed (at 0.001 s for $L = 0.01 \text{ kJ/kg}$ and at 0.10 s for $L = 100 \text{ kJ/kg}$) the temperature gradient normal to the solid surface is much larger for the larger latent heat case.

A layer of SPH particles on the free surface change to liquid as they attain the melting temperature uniformly and covers the solid particle. Due to capillary relaxation the liquid SPH particles near the free surface flow to the vicinity of the solid body, where they cool down. It is also possible that colder liquid SPH particles are transported back to the surface

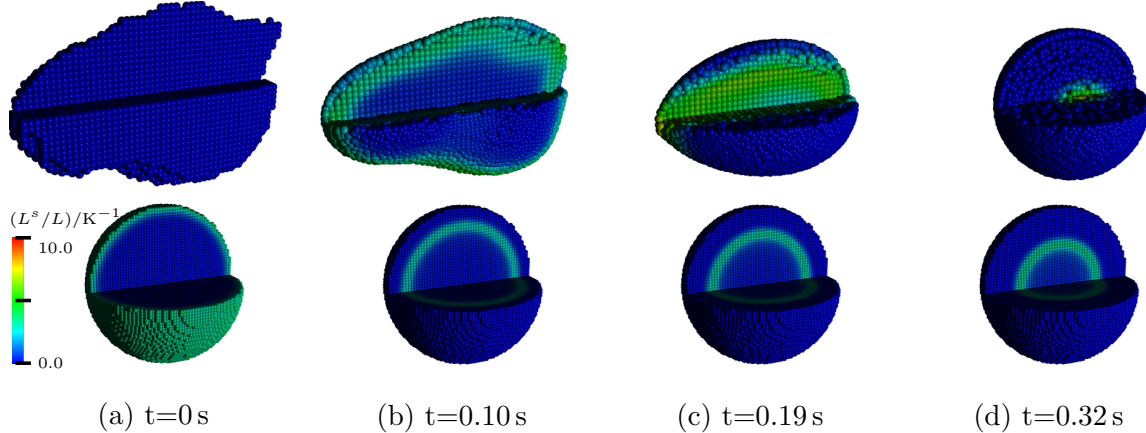


Figure 14: $L = 100.0 \text{ kJ/kg}$: Increase in heat capacity at the interface during the melting of the mill particle.

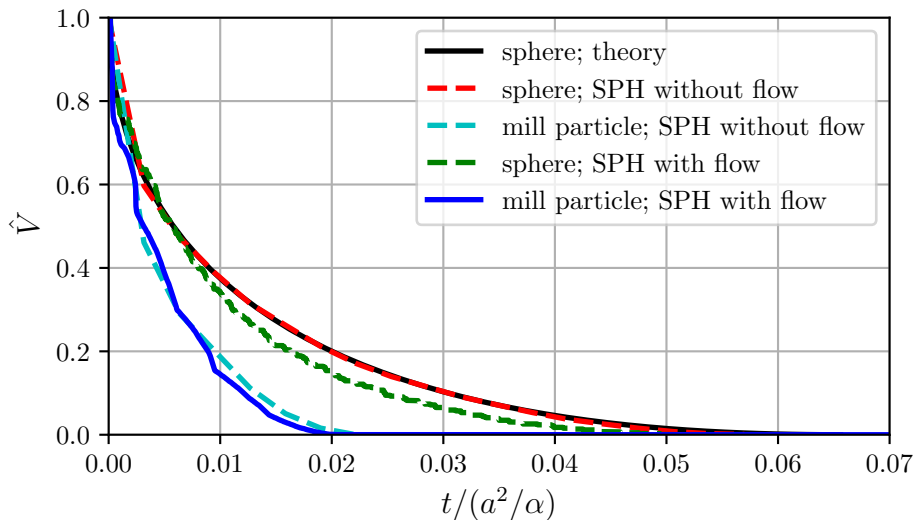


Figure 15: $L = 0.01 \text{ kJ/kg}$: Time variation of volume fraction of solid for a sphere and the mill particle of equal volume.

where they are heated up. This convective heat transfer is evident in the case of mill particle and is absent in the case of the static sphere. This can be clearly seen in Fig. 10d, where the mill particle melts much faster than the compared static sphere, where capillary relaxation isn't playing any role and the surface area to volume ratio is much smaller. In Figs. 13 and 14, the regions where latent heat is effective are shown. As the temperature rises, SPH particles enter the mushy region (Eq. 21), where the latent heat integrated over the mushy temperature range ($T_m - \Delta T < T < T + \Delta T_m$) is shown. From Figs. 13c and 14c, we see that the latent heat distribution near the interface is rather uniform.

To appreciate the effect of shape of the particle and its latent heat on the melting rate, the evolution of solid fraction of the unmelted solid are shown in Figs. 15, 16 and 17. In

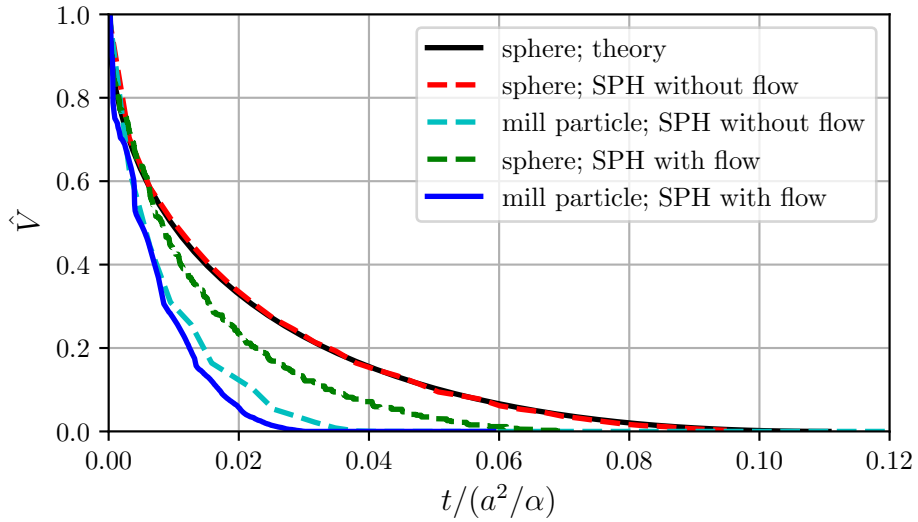


Figure 16: $L = 0.1 \text{ kJ/kg}$: Time variation of volume fraction of solid for a sphere and the mill particle of equal volume.

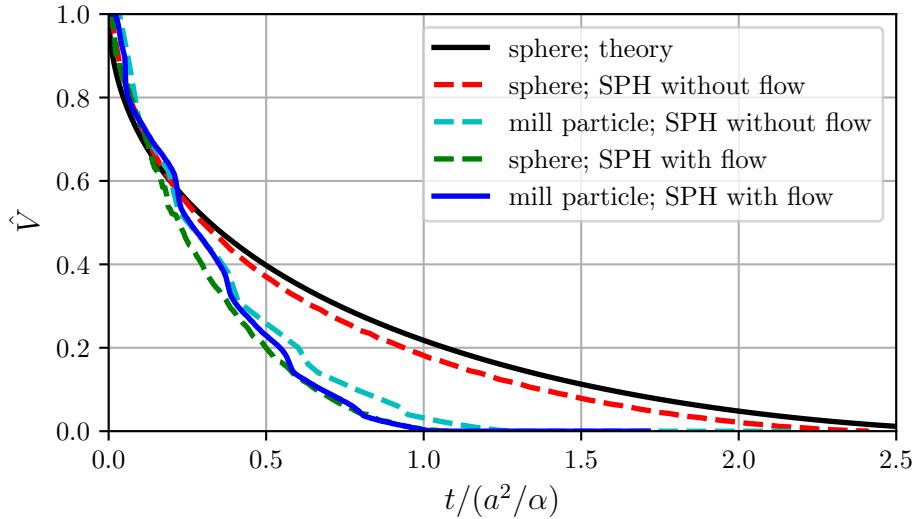


Figure 17: $L = 100 \text{ kJ/kg}$: Time variation of volume fraction of solid for a sphere and the mill particle of equal volume.

each of the three plots, a sphere with no melt flow (static melting), a sphere with melt flow (dynamic melting), the mill particle with no flow and the mill particle with melt flow are simulated. The axisymmetric theoretical result for each of these latent heat values [19] is shown by solid black lines and are essentially the same as in Fig. 7. For a low latent heat of 0.01 kJ/kg , the static and dynamic melting of the sphere evolves closely and is considerably different from those for the melting of the mill particle. The surface area of the mill particle

is 1.4 times that of the sphere of the same volume. The effect of the larger surface area reflects in the rate of melting of the mill particle. Since the capillary relaxation drives the flow in the arbitrary shaped mill particle, convection heat transfer also influences the melting process. Though the static melting compares well with the theoretical result, the dynamic melting of sphere deviates slightly from this melting rate. This could be because of flow related to the capillary relaxation due to noise in the simulation. One reason for this noise could be the spurious currents generated from the initial approximately spherical shape of the liquid layer. The spurious currents in initially spherical shapes in all numerical methods warrants separate attention [3]. In realistic scenarios, however, there could be noise that causes convective heat transfer even within a spherical drop of liquid due to other causes such as buoyancy and Gibbs-Marangoni effects. Convection in the dynamic sphere case is even more evident as the latent heat increases as seen in Figs. 16 and 17, the latter case where the dynamically melting sphere is closer to the melting evolution of the mill particle than the static case. Notwithstanding, the effect of shape (surface area) is evident from these plots. For the large latent heat case (Fig. 17 and 16), the mill particle (with and without flow) melts at a considerably faster rate than the static sphere. However the effect of convection due to flow in the mill particle causes difference in rate of melting between the mill particle with and without flow. The time for capillary relaxation compared to the time scale of phase change rate (which is dependent on the latent heat) is also the reason for increased convective heat transfer in the melt.

4.2. Agglomeration of a chain of melting solids

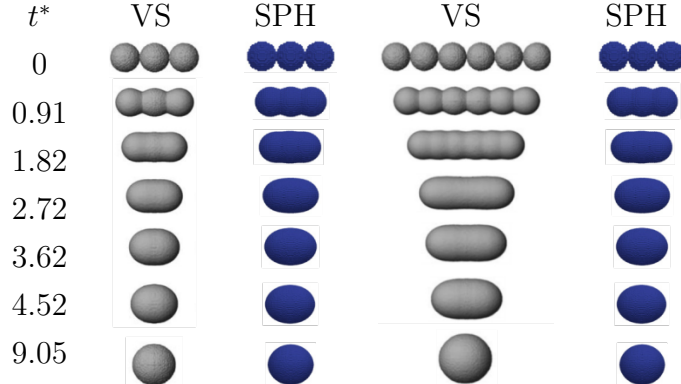


Figure 18: Shape evolution of agglomerate chains with three and six spheres. On the left side of each subfigure are the viscous flow sintering (VS) solutions by [15]. The right hand side of each of the case is the SPH simulation using only viscous flow assumption.

In order to motivate the application of the proposed SPH approach to understand the structural evolution of melting solids with realistic transport and thermal properties, we present the simulation of agglomeration of melting spheres. Such agglomeration is sometimes approximated as a slow viscous flow sintering phenomenon [15] in the low Reynolds number regime. In such an assumption, which is indeed valid for many engineering applications, a

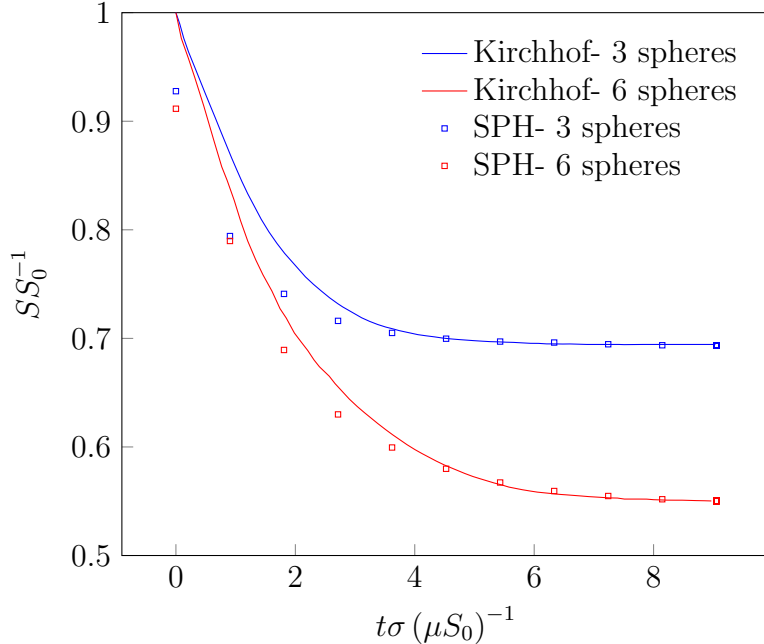


Figure 19: Dimensionless surface area evolution of agglomerate chains with three and six spheres. The surface area is normalized with the initial surface area S_0 of the primary particles. The normalized surface area determined by [15] are given as solid lines whereas the SPH viscous flow simulation results are shown as hollow circles.

non dimensional time can be defined as [15]

$$t^* = \frac{t\sigma}{\mu r_0}, \quad (26)$$

where σ is the surface tension, μ is the dynamic viscosity, r_0 is the radius of one primary sphere and t is the time. However, when the melt flow dynamics and heat transfer is fully coupled, the resulting structural change cannot be represented by a single non dimensional quantity. Hence we proceed to show the deviation of the surface evolution of melting solids from that of the viscous flow sintering assumption.

Initially, we perform 3D simulations of viscous flow sintering similar to that given in [15], using only viscous flow assumption in SPH and compare these results in Fig. 18 for both. A very good visual agreement is observed. Further, in Fig. 19, the evolution of dimensionless surface area of the agglomerate spheres is compared with the viscous sintering simulations and the quantitative agreement is clearly seen. We now simulate the spheres as solids with a finite latent heat, undergoing melting due to the heat transfer from ambience, through conduction and subsequent convection during flow of the melt. In table 2, we present the transport and thermal properties of the materials we simulate. Compared to the previous study of rounding of the mill particle, we have introduced discontinuities in the thermal properties between the solid and liquid phases in this case.

We present the melting dynamics of 3 spheres with a latent heat value of 100 kJ/kg. The phase, temperature and local latent heat are presented in Figs. 20, 21 and 22 respectively at

Table 2: Thermodynamic properties of the solid and liquid SPH particles as well as the ambient pseudoparticles for the melting of an agglomerate chain with three primary spheres.

Quantity	Value	Unit
σ	$7.12 \cdot 10^{-2}$	N m ⁻¹
Θ	30.00	°
μ	$1.00 \cdot 10^{-3}$	Pa s
ρ	$1.00 \cdot 10^3$	kg m ⁻³
T_0	1.00	K
T_m	1.15	K
k_s	2.14	W m ⁻¹ K ⁻¹
k_l	0.56	W m ⁻¹ K ⁻¹
C_s	$2.11 \cdot 10^3$	J kg ⁻¹ K ⁻¹
C_l	$4.22 \cdot 10^3$	J kg ⁻¹ K ⁻¹
L	1.00	J kg ⁻¹
T_{amb}	4.00	K
k_{amb}	0.56	W m ⁻¹ K ⁻¹
$c_{p, \text{amb}}$	$4.22 \cdot 10^3$	J kg ⁻¹ K ⁻¹

different time instances. After 0.0025 s, a thin layer of liquid is formed on the spheres, which coalesce with the adjacent spheres. The resulting fluid-solid interaction results in a complex free surface evolution, remarkably different from the assumption of viscous flow sintering in Fig. 18. Up to 0.0089 s, the overall shape remains rather symmetric. A marked instability is observed at 0.0521 s as the numerical errors serve as perturbation, resulting in a sudden decrease in surface area. From this point, the overall shape remains a sphere even though the solids have not all melted. At 0.1341 s, two out of the three primary spheres are completely molten, implying that the non-linear motion of the spheres also affect heat transfer in the bulk of the material. This clearly shows that the presence of yet to melt solids as suspensions influencing the shape evolution of the melt itself.

In order to appreciate the influence of the fluid–solid interaction and the capillary viscous flow on the shape evolution, we present two simulations with varying thermal and transport properties resulting in shape evolution in comparable time instances, in Fig. 23. These properties are chosen in such a way that the shape evolves into a sphere in approximately same time scales. Multiphysics simulation shown on the right column of this figure uses a viscosity coefficient that is 1000 times smaller than the viscosity used in the viscous flow sintering simulation shown on the left column. Meanwhile, a realistic latent heat value of 100 kJ/kg is used for multiphysics simulation in the right column to slow down the phase change and thereby the rounding process. At these values, the shapes evolve at comparable rates as seen in Fig. 23. Since the fluid is not all molten for the given time instances, the fluid-solid interaction results in complex shapes, often resulting in low aspect ratio shapes compared to the result from the linear assumptions. In microstructure evolution in additive manufacturing, including the influence of such fluid-solid interaction would provide insight into the melt flow, pore evolution, defect formations and also in determining optimal layer thickness during the powder spreading processes.

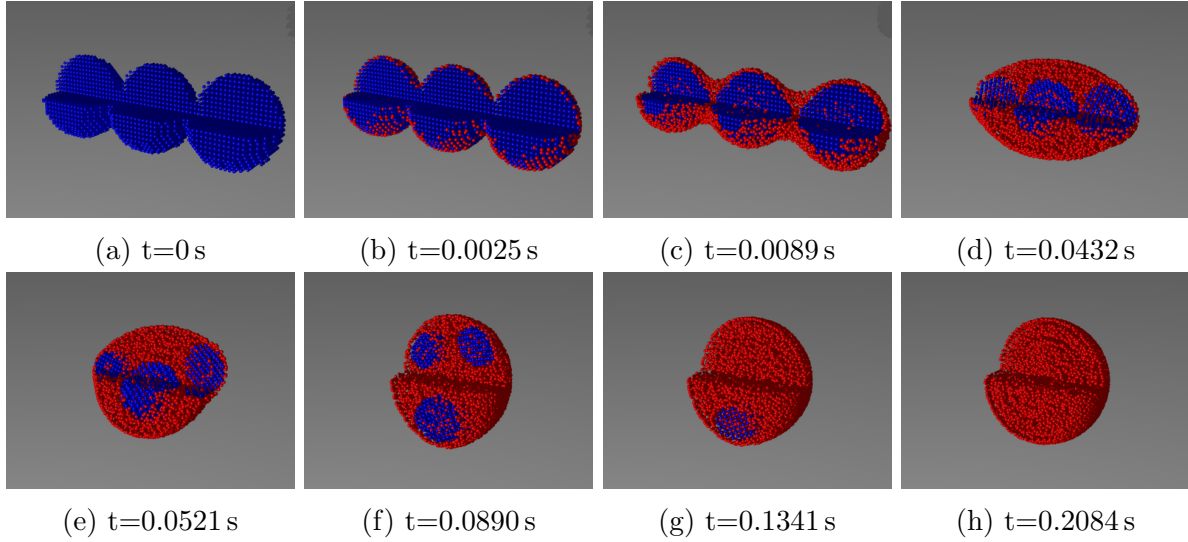


Figure 20: Representation of the solid-liquid phase change of an agglomerate chain with three primary particles. Blue colored SPH particles denote solid and red colored SPH particles liquid state. Melting occurs until all SPH particles are in the liquid state and form a sphere.

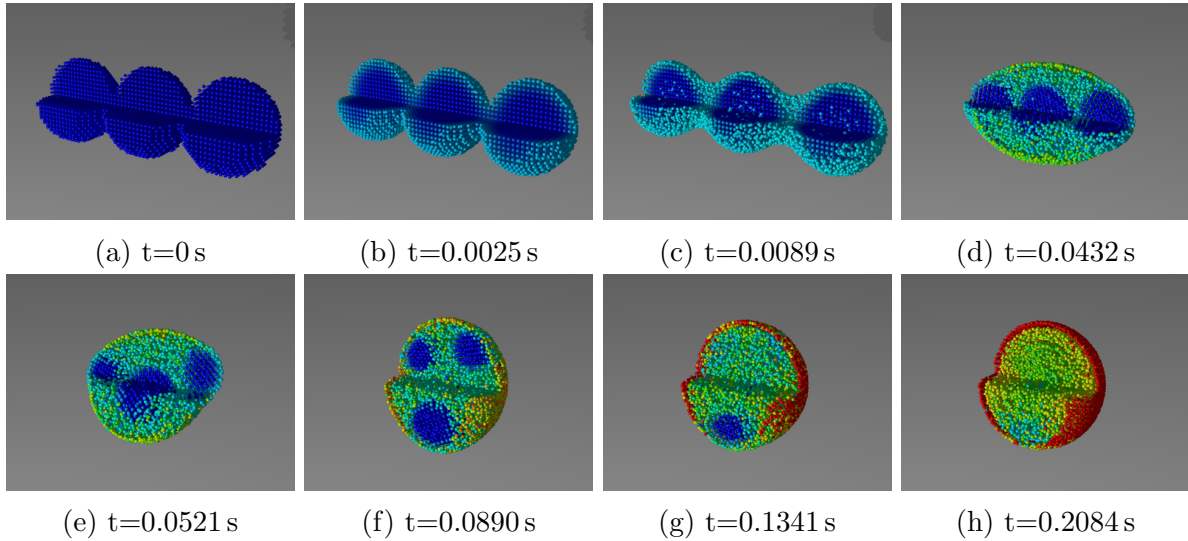


Figure 21: Temperature profile of three primary particles forming an agglomerate chain and liquid state particles formed during the melting process. The temperature takes values between 1.0 K (blue colored) and 3.034 K (red colored).

5. Conclusions

A multiphysics SPH method that couples heat transfer, phase change and capillary flow solver is presented in the context of Incompressible Smoothed Particle Hydrodynamics. A constant volume melting model is implemented. The melting model is based on a specific heat capacity that increases additively by the latent heat of the material, near the melting interface and at temperatures close to the melting point. Heat transfer across the free

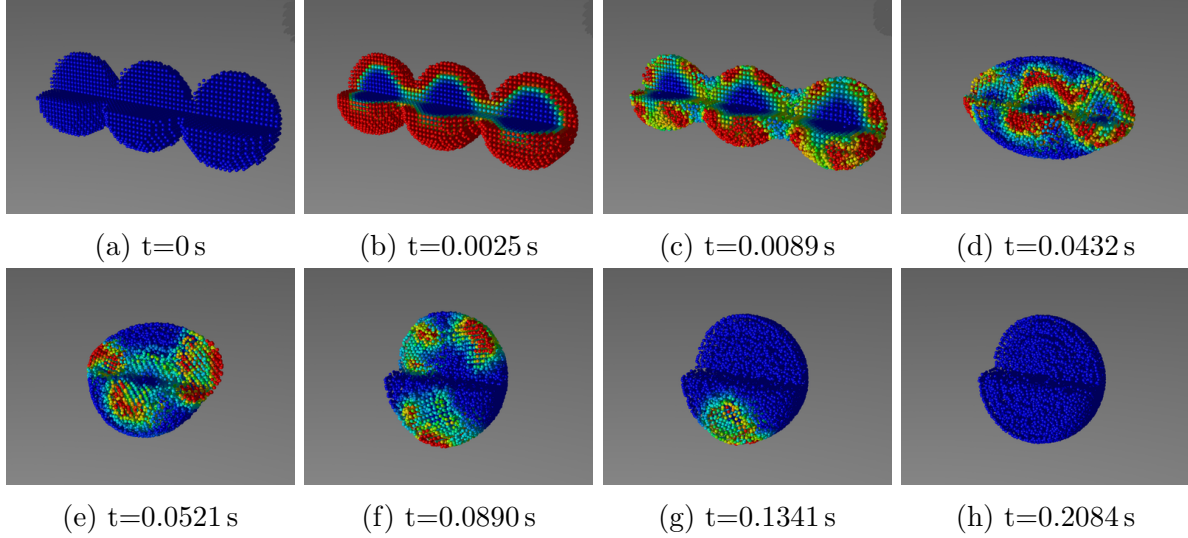


Figure 22: Representation of the regions in which the SPH particles are located in the temperature range of the phase change. The effect of latent heat is normalized and has its greatest effect in red-colored areas. Blue colored SPH particles are outside the mushy-region for the phase change and experience no effect due to the latent heat.

surface through a semi-analytic Dirichlet BC across the free surface allows the simulation of complex shaped bodies. The method is carefully validated against theoretical models on melting and conduction heat transfer. leads to spurious velocities increasing the convective thermal transport compared to theory.

The method is first applied to study the influence of particle shape on its surface evolution during heating and subsequent melting of the particle. We simulate melting process across a range of latent heat values and show that at high latent heat values the melting process evolves substantially differently from assumptions of a spherical shape. A non spherical shape, owing to its increased surface area melts faster than a sphere of the same volume. Additionally, capillary flow of the melt further increases the heat transfer due to the flow within the melt and accelerates the melting process. However the influence of spurious currents, typical of numerical capillary flow simulations, is also seen in the simulations of melting spheres. This persistent issue requires further detailed attention.

The method is then applied to the study of agglomeration of a chain of particles that undergo melting. The results are compared against simulations that assume viscous flow sintering. We show that when unmelted solid particles are present (owing to large latent heat of melting of the material), the evolution of shape of the agglomerate follows a highly non-linear path due to the fluid–solid interaction within the body of the melt. Thus, a case is made for the method’s applicability to microstructure studies in additive manufacturing where time scales of the flow and phase change are comparable.

Additional effects such as Marangoni forces and recoil pressure (in case of metals) also play an important role in additive manufacturing. Modeling of these phenomena in the context of SPH and their compounded effect on the dynamics of melting require elaborate study. In this work, we have used representative transport and thermal properties. However

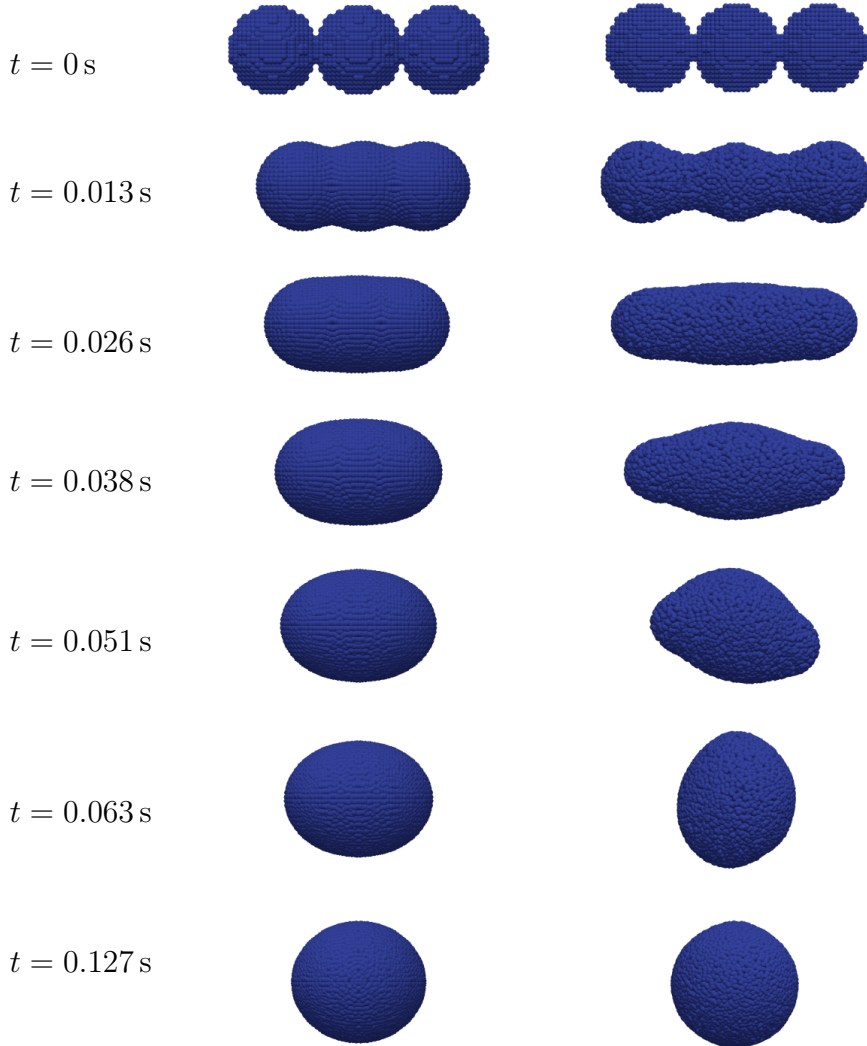


Figure 23: Comparison of the coalescence agglomerates. Left column shows the viscous flow assumption whereas the right column shows the melting process of initially solid particles.

this doesn't span the entire range of properties encountered in real applications. For example, high viscosities encountered in additive manufacturing using polymers would require implicit computation of viscosities. Simulations with high latent heat values require adaptive time stepping to reduce computational costs. These improvements in computational efficiency will enable simulations of large number of particles needed for relating microstructure to bulk properties of manufactured parts.

Acknowledgements

The authors gratefully acknowledge the support of the Cluster of Excellence Engineering of Advanced Materials, ZISC, FPS and the Collaborative Research Center SFB814 funded by the German Science Foundation (DFG), and the Indo-German Partnership in Higher Education Program (IGP) 2016, funded by DAAD-UGC.

References

- [1] Adami, S., Hu, X., Adams, N., 2010. A new surface-tension formulation for multi-phase SPH using a reproducing divergence approximation. *J. Comput. Phys.* 229 (13), 5011–5021.
- [2] Beckett, G., Mackenzie, J. A., Robertson, M., 2001. A moving mesh finite element method for the solution of two-dimensional Stefan problems. *J. Comput. Phys.* 168 (2), 500–518.
- [3] Bogner, S., Rüde, U., Harting, J., 2016. Curvature estimation from a volume-of-fluid indicator function for the simulation of surface tension and wetting with a free-surface lattice Boltzmann method. *Phys. Rev. E* 93 (4), 043302.
- [4] Bonacina, C., Comini, G., Fasano, A., Primicerio, M., 1973. Numerical solution of phase-change problems. *Int. J. Heat Mass Transfer* 16 (10), 1825–1832.
- [5] Chen, Q., Guillemot, G., Gandin, C.-A., Bellet, M., 2017. Three-dimensional finite element thermomechanical modeling of additive manufacturing by selective laser melting for ceramic materials. *Addit. Manuf.* 16, 124–137.
- [6] Das, S., 2003. Physical aspects of process control in selective laser sintering of metals. *Adv. Eng. Mater.* 5 (10), 701–711.
- [7] Ehigiamusoe, N. N., Maxutov, S., Lee, Y. C., 2018. Modelling surface tension of two-dimensional droplet using smoothed particle hydrodynamics. *Int. J. Numer. Methods Fluids*.
- [8] Farrokhpahanah, A., Bussmann, M., Mostaghimi, J., 2017. New smoothed particle hydrodynamics (sph) formulation for modeling heat conduction with solidification and melting. *Numer. Heat Transfer, Part B* 71 (4), 299–312.
- [9] Gingold, R. A., Monaghan, J. J., 1977. Smoothed particle hydrodynamics - theory and application to non-spherical stars. *Mon. Not. R. Astron. Soc.* 181, 375–389.
- [10] Guo, N., Leu, M. C., 2013. Additive manufacturing: technology, applications and research needs. *Front. Mech. Eng.* 8 (3), 215–243.
- [11] Gürtler, F.-J., Karg, M., Leitz, K.-H., Schmidt, M., 2013. Simulation of laser beam melting of steel powders using the three-dimensional volume of fluid method. *Physics Procedia* 41, 881–886.
- [12] Hirt, C. W., Nichols, B. D., 1981. Volume of fluid (vof) method for the dynamics of free boundaries. *J. Comput. Phys.* 39 (1), 201–225.
- [13] Hsiao, J., Chung, B. T., 1986. An efficient algorithm for finite element solution to two-dimensional heat transfer with melting and freezing. *J. Heat Transfer* 108 (2), 462–464.
- [14] Hsiao, J.-S., 1983. Numerical and analytical analyses of heat transfer with ablation in a two-dimensional region. Ph.D. thesis, University of Akron.

- [15] Kirchhof, M., Schmid, H.-J., Peukert, W., 2009. Three-dimensional simulation of viscous-flow agglomerate sintering. *Physical Review E* 80 (2), 026319.
- [16] Kreyszig, E., 2010. Advanced engineering mathematics. John Wiley & Sons.
- [17] Lucy, L. B., 1977. A numerical approach to the testing of the fission hypothesis. *Astron. J.* 82, 1013–1024.
- [18] May, D., Monaghan, J., 2003. Can a single bubble sink a ship? *Am. J. Phys.* 71 (9), 842–849.
- [19] McCue, S. W., Wu, B., Hill, J. M., 2008. Classical two-phase Stefan problem for spheres. In: *Proc. R. Soc. London, Ser. A. Vol. 464*. The Royal Society, pp. 2055–2076.
- [20] Mittal, R., Iaccarino, G., 2005. Immersed boundary methods. *Annu. Rev. Fluid Mech.* 37, 239–261.
- [21] Monaghan, J. J., 1992. Smoothed particle hydrodynamics. *Annual review of astronomy and astrophysics* 30, 543–574.
- [22] Morris, J. P., Fox, P. J., Zhu, Y., 1997. Modeling low reynolds number incompressible flows using sph. *J. Comput. Phys.* 136 (1), 214–226.
- [23] Nair, P., Pöschel, T., 2018. Dynamic capillary phenomena using incompressible SPH. *Chem. Eng. Sci.* 176, 192–204.
- [24] Nair, P., Tomar, G., 2014. An improved free surface modeling for incompressible sph. *Comput. Fluids* 102, 304–314.
- [25] Nair, P., Tomar, G., 2015. Volume conservation issues in incompressible smoothed particle hydrodynamics. *J. Comput. Phys.* 297, 689–699.
- [26] Pasandideh-Fard, M., Mostaghimi, J., 1996. Droplet impact and solidification in a thermal spray process: droplet-substrate interaction. *Thermal spray: Practical Solutions for Engineering Problems*, CC Berndt (Ed.), Pub. ASM International, Material Park, Ohio-USA, 637–646.
- [27] Rathjen, K. A., Jiji, L. M., 1971. Heat conduction with melting or freezing in a corner. *J. Heat Transfer* 93 (1), 101–109.
- [28] Riedlbauer, D., Steinmann, P., Mergheim, J., 2014. Thermomechanical finite element simulations of selective electron beam melting processes: performance considerations. *Comput. Mech.* 54 (1), 109–122.
- [29] Rowlinson, J. S., Widom, B., 2013. Molecular theory of capillarity. Courier Corporation.
- [30] Schoinchoritis, B., Chantzis, D., Salonitis, K., 2017. Simulation of metallic powder bed additive manufacturing processes with the finite element method: A critical review. *Proceedings of the Institution of Mechanical Engineers, Part B: Journal of Engineering Manufacture* 231 (1), 96–117.

- [31] Sleijpen, G. L., Van der Vorst, H. A., Fokkema, D. R., 1994. BiCGstab (l) and other hybrid Bi-CG methods. *Numerical Algorithms* 7 (1), 75–109.
- [32] Stewartson, K., Waechter, R., 1976. On Stefan's problem for spheres. In: *Proceedings of the Royal Society of London A: Mathematical, Physical and Engineering Sciences*. Vol. 348. The Royal Society, pp. 415–426.
- [33] Szewc, K., Pozorski, J., Minier, J.-P., 2012. Analysis of the incompressibility constraint in the smoothed particle hydrodynamics method. *Int. J. Numer. Methods Eng.* 92 (4), 343–369.
- [34] Tartakovsky, A. M., Panchenko, A., 2016. Pairwise force smoothed particle hydrodynamics model for multiphase flow: surface tension and contact line dynamics. *J. Comput. Phys.* 305, 1119–1146.
- [35] Thomas, B., Samarasekera, I., Brimacombe, J., 1984. Comparison of numerical modeling techniques for complex, two-dimensional, transient heat-conduction problems. *Metall. Mater. Trans. B* 15 (2), 307–318.
- [36] Voller, V., Cross, M., 1981. Accurate solutions of moving boundary problems using the enthalpy method. *International journal of heat and mass transfer* 24 (3), 545–556.
- [37] Voller, V. R., Prakash, C., 1987. A fixed grid numerical modelling methodology for convection-diffusion mushy region phase-change problems. *Int. J. Heat Mass Transfer* 30 (8), 1709–1719.
- [38] Zhang, M., 2010. Simulation of surface tension in 2D and 3D with smoothed particle hydrodynamics method. *J. Comput. Phys.* 229 (19), 7238–7259.